Glassy nature and glass-to-crystal transition in the binary metallic glass CuZr

Zi-Yang Wei, Cheng Shang, Xiao-Jie Zhang, and Zhi-Pan Liu[*]

Collaborative Innovation Center of Chemistry for Energy Material, Key Laboratory of Computational Physical Science (Ministry of Education), Shanghai Key Laboratory of Molecular Catalysis and Innovative Materials, Department of Chemistry, Fudan University, Shanghai 200433, China

The prediction for the stability of glassy material is a key challenge in physical science. Here, we report a theoretical framework to predict the glass stability based on stochastic surface walking global optimization and reaction pathway sampling. This is demonstrated by revealing for the first time the global potential energy surface (PES) of two systems, CuZr binary metallic glass and nonglassy pure Cu systems, and establishing the lowest energy pathways linking glassy/amorphous structures with crystalline structures. The CuZr system has a significant number of glassy structures on PES that are $\sim$0.045 eV/atom above the crystal structure. Two clear trends are identified from global PES in the glass-to-crystal transition of the CuZr system: (i) the local Zr-Cu coordination (nearest neighbor) increases, and (ii) the local Zr bonding environment becomes homogeneous. This allows us to introduce quantitative structural and energetics conditions to distinguish the glassy structures from the crystalline structures. Because of the local Zr-Cu exchange in the glass-to-crystal transition, a high reaction barrier ($>$0.048 eV/atom) is present to separate the glassy structures and the crystals in CuZr. By contrast, the Cu system, although it does possess amorphous structures that appear at much higher energy ($\sim$0.075 eV/atom) with respect to the crystal structure, has very low reaction barriers for the crystallization of amorphous structures, i.e. $<$0.011 eV/atom. The quantitative data on PES now available from global optimization techniques deepens our understanding on the microscopic nature of glassy material and might eventually facilitate the design of stable glassy materials.

I. INTRODUCTION

Metallic glasses [1,2], for their unusual magnetic [3] and mechanic properties [4,5], emerge as an important class of materials with important applications [3,5–8]. CuZr binary alloy, as a typical metallic glass former, has received much recent attention since the discovery of the first $Cu_{64.5}Zr_{35.5}$ bulk metallic glass in 2004 [9–11]. The glassy samples with other compositions, such as $Cu_{50}Zr_{50}$ [12] and $Cu_{46}Zr_{54}$ [13], were later reported, and it was found that there is a wide glass former range, 30–70% Zr composition [11], for the CuZr system. It is, however, a great challenge for both experiment and theory [14–21] to understand the nature of glassy states. The prediction of the glass forming ability in general is an urgent task in material science. Fundamentally, this would require a detailed knowledge of the multidimensional potential energy surface (PES) that contains a huge number of glassy minima, crystalline minima, and the reaction pathways linking them [22]. Because of the slow kinetics and the large degrees of freedom in the glass-to-crystal transformation, current theoretical techniques are frustrated in exploring the PES and quantifying the transition kinetics of crystallization.

Great efforts have been devoted to probe the structure of CuZr metallic glass. Li *et al.* [23], using reverse Monte Carlo (RMC) to fit experimental data, discovered that special icosahedronlike clusters are dominant in $Cu_{50}Zr_{50}$, especially Cu-centered $\langle 0,2,8,2 \rangle$ and $\langle 0,0,12,0 \rangle$ Voronoi clusters [see Fig. 1(a)]; it is suggested that these clusters cause the local dense packing [20] in the glassy phase. (The Voronoi index [24] is a series of numbers $\langle n_3, n_4, n_5, n_6, \dots \rangle$, where n_i denotes

the number of i-edged faces on the polyhedron.) Theoretical simulations based on long-time (nanoseconds) molecular dynamics (MD) have also been utilized to understand the PES of a glassy system and track the structure evolution during vitrification from liquid to glass [13,25–27]. For example, Sastry *et al.* [28] utilized the inherent structures of a model Lennard-Jones (LJ) system obtained from MD trajectories at different cooling rates to analyze the glassy features and revealed the dynamics of glass transition can be related to the topographic features of the energy landscape [28–30]. Fan *et al.* investigated the thermally activated deformation of the $Cu_{56}Zr_{44}$ system [27] and showed that the cascade deformation is more frequently observed in the fast quenched system due to the higher density of local minima. To reveal the structural origin for glass transition, Cheng *et al.* [25] showed that the presence of Cu-centered $\langle 0,0,12,0 \rangle$ clusters in metallic glass causes the slow dynamics and contributes greatly to the glass forming ability in $Cu_xZr_{100-x}(x = 46-65)$. These findings are consistent with the topological theory proposed by Miracle, emphasizing the role of densely packed local clusters in forming metallic glass [19,20]. Similar conclusions were drawn in other metallic glasses, including $Cu_{46}Zr_{54}$ [13] and $Cu_{64}Zr_{36}$ [26], although the relative portion of different Voronoi clusters differs from paper to paper.

On the other hand, the stability of the glassy state, a key property of glassy materials, is extremely difficult to predict, which is measured by the kinetics of glass-to-crystal transformation. Experimentally, Kalay *et al.* [31] observed that, for the $Cu_{50}Zr_{50}$ metallic glass, the initial devitrification involves the formation of three coexisting phases, including $Cu_{10}Zr_7$, $CuZr_2$, and CuZr (B2 phase). They propose that the nucleation of the B2 phase initiates the crystallization response followed by rapid formation of more stable $Cu_{10}Zr_7$ and $CuZr_2$
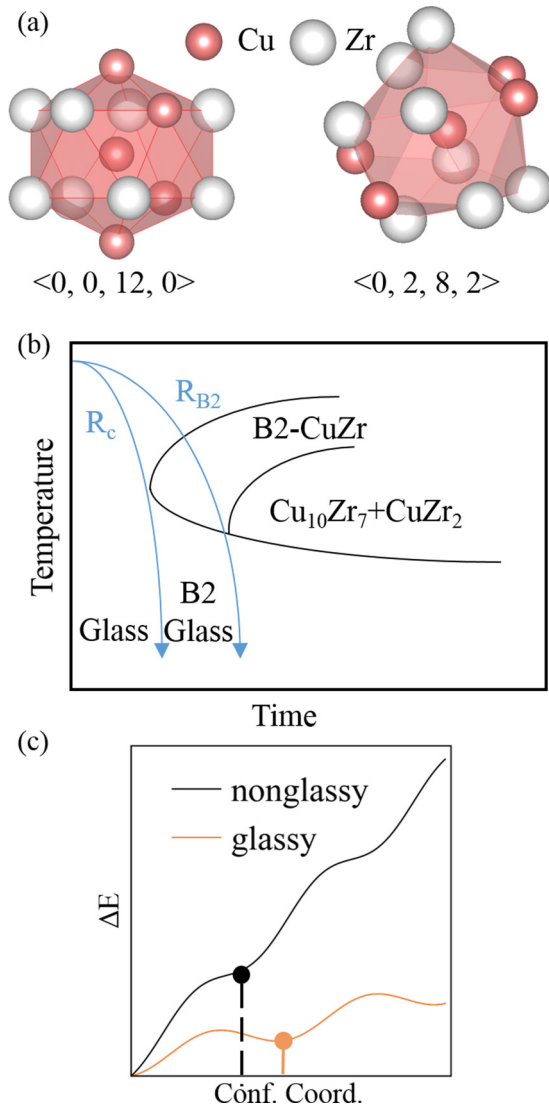
[*]zpliu@fudan.edu.cn

FIG. 1. (a) Typical Cu-centered polyhedral clusters in CuZr metallic glass, icosahedron $\langle 0,0,12,0\rangle$ and distorted icosahedron $\langle 0,2,8,2\rangle$. (b) Schematic diagram for the continuous cooling transformation of CuZr-based metallic glass [32], showing that two different cooling rates, R_c and R_{B2} curves, will result in either the glass or the mixed (glass + B2) products. (c) Conceptual 1D global PES showing the difference between glassy and nonglassy systems. The x and y axes represent the configurational coordinate to distinguish structures on PES and the relative energy, respectively.

phases, as schematically shown in Fig. 1(b) [32]. On the theory side, the conceptual tools based on global PES were often utilized to understand qualitatively the glass transformation. As the one-dimensional (1D) global PES schematically shown in Fig. 1(c), it was accepted [33] that the glassy systems have local minima with similar energies, which are separated by relatively high barriers. The PES for the crystallization of model atomic and molecular glass formers within fixed volume have been studied in detail using discrete path sampling by Calvo *et al.* [34], de Souza and Wales [35–37], and Niblett *et al.* [38], who correlate the crystallization kinetics with the coordination change of atoms (e.g. in the cage breaking event). For nonglassy systems, by contrast, there are much fewer

minima in the amorphous states, and their energy differences with respect to the global minimum (GM; the crystalline structure) are large, which helps to reduce the barrier in crystallization according to the Tomlinson model [39,40].

However, such conceptual global PES pictures were not yet confirmed by modern computational simulations in real materials that are frustrated to explore a large area of PES due to the high barrier of the solid transition reaction and the limited timescale in simulation. This has hindered establishing a deeper understanding on the glassy nature of material from theory. A general approach based on global PES is highly desirable for predicting the glass forming ability of solids and for high-throughput material design.

By exploiting novel global optimization techniques, the stochastic surface walking (SSW) method, we here aim to establish the global PES for a real binary metallic glass, the CuZr system, and reveal the glass-to-crystal transition kinetics. We introduce quantitative measures to distinguish CuZr glassy structures from the crystalline structures and utilize the SSW-based iterative reaction sampling method to determine the lowest energy pathway of crystallization. The nonglassy Cu system is investigated for comparison. We show that, with the global PES data, it is now feasible to predict the glassy nature of a real material and thus the high-throughput material design of a novel glassy material is within reach.

II. THEORETICAL METHODS

A. Reaction pathway sampling based on SSW method

In this paper, we utilized the SSW method [41–43] to explore PES and the SSW reaction sampling method [44] to identify the low-energy pathways (see Supplemental Material Part 1 [45] for more details about the SSW reaction sampling method [41–44,46–53]). Here, we briefly describe SSW as follows, and the detailed algorithm can be found in our previous papers [41–43]. The SSW method is an unbiased PES exploration method, originating from the bias-potential-driven constrained Broyden dimer method [46] for transition state (TS) searching developed in the group. In the SSW method, each SSW step is composed of a climbing procedure and a relaxation procedure to perturb the structure from one minimum to another. The climbing procedure involves adding consecutively Gaussian bias potentials to surmount the barrier of the reaction and repeated local relaxation. The relaxation procedure removes all the bias potentials and utilizes an unconstrained quasi-Newton Broyden-Fletcher-Goldfarb-Shanno (BFGS) optimization to identify local minimum. At the end of each SSW step, a metropolis MC [54] scheme is utilized to determine whether the new minimum is accepted or refused. In this paper, we utilized the following parameters for our SSW simulation: the Gaussian width of 0.5 Å; the number of the Gaussian is 7 for atoms and 10 for cells; MC temperatures with 1000 and 20000 K for the CuZr system and 100000 K for the Cu system.

With all important minima identified from the global PES, we can then utilize the SSW reaction sampling method to search for the lowest energy pathway linking a pair of minima on PES. Our previous paper has developed a SSW reaction sampling method for finding the lowest energy pathway

of elementary reactions [44], as demonstrated in molecular reactions and crystal phase transitions [47,55,56]. The method consists of two parts: the SSW method [41–43], which explores the PES unbiasedly and searches for possible pathways; and the double-ended surface walking (DESW) method [52,53], which locates the TS of the pathway, where the TS is a saddle point on PES with one and only one negative frequency. The DESW method has been described in our previous papers for both aperiodic [40] and periodic systems [52,53]. For studying the glass-to-crystal transition, this paper extends the original version of SSW reaction sampling to allow for treating efficiently multiple-step reactions (i.e. with multiple TSs). This approach is based on massive iterative calculations of elementary steps sampled from SSW trajectories, as explained in the following.

For multiple-step reactions with multiple reaction channels in between **A** and **B** minima on PES, i.e. **A** → **B** with i, j being possible intervening minima, we can separate the pathway into pairwise linkages **A** → i, i → j and j → **B**. Each lowest energy pathway, min(**A** → i), min(i → j) and min(i → **B**), can be revealed using SSW reaction sampling by sampling intervening i and j states. It is therefore critical to identify the correct intervening minima that are present in the lowest energy pathway. This can be solved using an iterative scheme. In each cycle of iteration, the new intervening minima that can connect **A** to **B** will be sampled using SSW reaction sampling, from which a number of low-energy pathways are determined and collected according to the two-state rate theory [57]. From these low-energy pathways, the intervening minima that have not been sampled previously are identified and fed as input for the next cycle. The initial intervening minima (at cycle 1) can be quite arbitrary as long as they form linkages from **A** to **B**. In the whole process, the connectivity between adjacent minima on PES will be established or updated using the lowest energy pathway.

B. Calculation details for CuZr and the pure Cu system

All structures were calculated using the Large-scale Atomic/Molecular Massively Parallel Simulator (LAMMPS) package [58] in the periodic boundary condition. All the structures are optimized using the quasi-Newton BFGS method until the maximal force component on an atom is below 0.001 eV/Å and the stress is below 0.001 GPa. The Voronoi tessellation [24] was performed using the Voronoi tool package of LAMMPS. The Steinhardt-type order parameter [59] [see Eq. (1)] was utilized to distinguish the structures on the global PES, which considers only the first shell bondings

$$\mathrm{OP}_l = \left(\frac{4\pi}{2l+1} \sum_{m=-l}^{l} |\overline{Y_{lm}(\mathbf{n})}|^2 \right)^{1/2}. \qquad (1)$$

In Eq. (1), Y_{lm} is the spherical harmonic function of degree l and order m, $\mathbf{n}$ is the normalized direction between all bonded atoms, and the bar over Y_{lm} means the average over all bonded atoms. The Steinhardt-type order parameter describes the bond-oriented ordering around one atom.

Due to the enormous number of structures on the global PES, we utilize the embedded atom method (EAM) potential to combine with SSW global optimization for minima sampling

and reaction pathway search. Typically, the number of minima visited by SSW to establish the global PES is more than 10^5, and that for searching the lowest barrier pathway between a glassy structure and a crystal structure is more than 10^6.

The interaction in the CuZr system is described by the EAM potential developed by Cheng *et al.* [60], a widely used empirical model for describing interatomic interactions in metals and alloys [61]. The CuZr EAM potential fits the *ab initio* MD data and has been proved to predict the properties of crystalline phases and glassy states of CuZr correctly, which are consistent with the *ab initio* data [60] or experimental data [62,63].

We have systematically studied the CuZr system in different supercells up to 32 atoms per supercell, and the reported data in this paper is carried out in a 16-atom supercell, containing 8 Cu atoms and 8 Zr atoms. The global PES for a 32-atom supercell is shown in Supplemental Material Fig. S1 [45] for comparison with the one in Fig. 2 from a 16-atom supercell. We show that the 16- and 32-atom supercell calculations give the same energy gap between crystalline structures and glassy structures, and the same trend for the structural evolution from the crystalline structures to the glassy structures.

For the pure Cu system, we also utilized a well-established EAM potential for Cu, developed by Mendelev *et al.* [64] to fit *ab initio* data. The benchmark of the EAM results with *ab initio*/experimental data can be found in Ref. [64]. We also tested the Cu potential taken from the CuZr potential [60]. Our SSW simulation shows that the two different Cu potentials produce similar overall global PES (see Supplemental Material Fig. S2 for discussions [45]) and the coordination characteristics, which suggests that the results obtained from this paper are not sensitive to the choice of Cu potential.

Similarly, we studied different supercell sizes for the Cu system, including 16, 32, and 48 atoms per cell. The reported data in this paper contain 32 atoms per supercell. The larger supercell required for the Cu system than the CuZr system is in fact related to the nonglassy nature of Cu, which has much fewer minima on the PES and is facile to crystallization. Only in the large 32-atom supercell can we find a large number of structures with clear amorphous characteristics, as discussed in Fig. 5. In Supplemental Material Fig. S3 [45], we also compared the global PESs from 32- and 48-atom SSW simulations. We found that, while the 48-atom system contains much more amorphous structures than expected due to the larger degrees of freedom, the essential energetics and structural features for the amorphous structures are largely the same in both systems. To achieve an efficient pathway sampling, we chose the Cu system with 32 atoms per cell as the model for a nonglassy system to compare with the glassy CuZr system.

III. RESULTS

A. Global PES of the Cu$_{50}$Zr$_{50}$ glassy system

Our paper starts by exploring CuZr minima on the PES using the SSW method. We are aiming to achieve two objectives: (i) to reveal the crystalline phases, and (ii) to identify the nature of glassy structures. The SSW exploration utilizes a 16-atom supercell with 1:1 Cu Zr ratio and visits 10^5
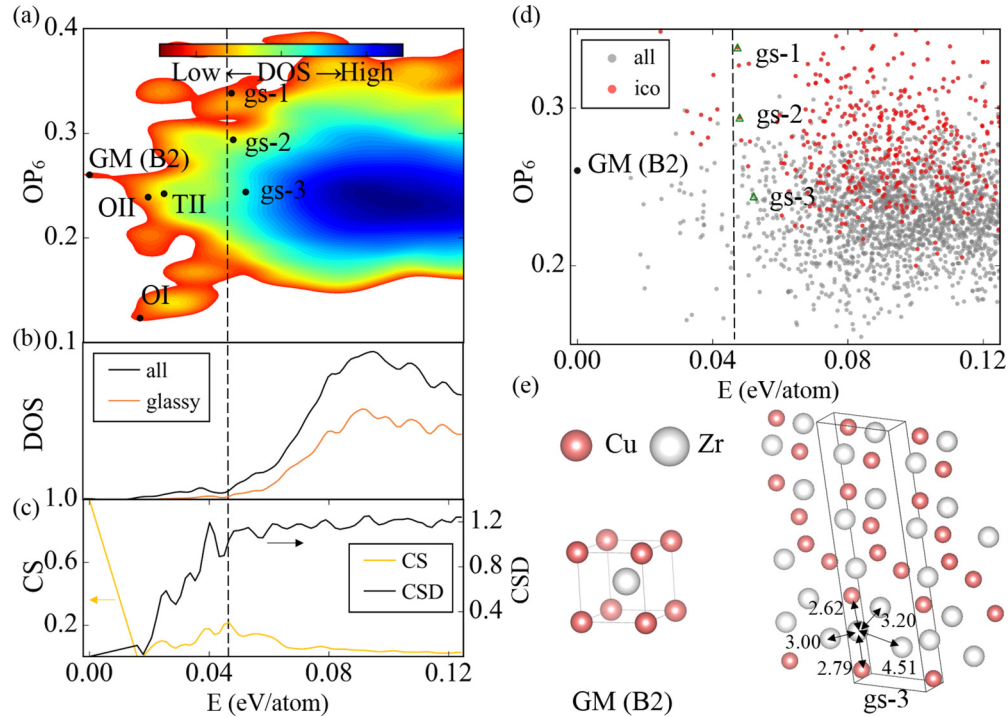
FIG. 2. (a) Global PES of the CuZr system (16-atom supercell), where the energy of structure (minimum) is plotted against the order parameter OP_6 [see Eq. (1)]. The color indicates the DOS of minima. (b) 1D DOS profile for all CuZr structures as appeared in (a), and for the selected structures satisfying the structural conditions of Eqs. (6) and (7). (c) CS and CSD [see Eqs. (3) and (4)] profile of the CuZr system to show the structure evolution from crystal to glass. The dashed line indicates the energy condition to separate the glassy structures from the crystalline structures. (d) Structures on the global PES with (red dots) and without (gray dots) icosahedral $\langle 0,0,12,0 \rangle$ clusters. (e) Atomic structure for the crystal B2 phase, the GM, and a representative glassy structure, gs-3 in (a). The distances (Å) of Zr-Cu and Zr-Zr bonds around the Zr atom with lowest Cu coordination are shown.

minima on PES. From these minima, we can identify 3021 distinct minima, which differ in the energy (>0.001 eV/atom), the space group, and Steinhardt-type order parameter [>0.002 for every degree $l = 2, 4$, and 6, see Eq. (1) in Sec. II B] [59].

In Fig. 2(a), we have shown the contour plots for the density of states (DOS) of all distinct minima of CuZr, where the energy of each structure (eV/atom) is plotted against its Steinhardt-type order parameter with degree $l = 6(OP_6)$. The 1D DOS for the minima is shown in Fig. 2(b) together with the contour plot.

On the CuZr global PES, we can identify a number of high-symmetry crystalline structures. The most stable crystal phase is the B2 phase [$Pm\bar{3}m$, #221, Fig. 2(e)], which is set as energy zero reference. For convenience, we term this structure as GM, which is the most stable structure in our search. In the B2 phase, each Cu is surrounded by eight Zr atoms, and each Zr is also surrounded by eight Cu atoms. There are also less stable crystalline minima (the structures of them are shown in Supplemental Material Fig. S4 [45]), such as the orthorhombic structure OI (*Cmcm* #63), the orthorhombic structure OII (*Imma* #74), and the tetragonal structure TI (*P4mm* #99). These less stable crystalline structures locate in the energy window <0.02 eV/atom, as indicated in Fig. 2(a).

It should be mentioned that the EAM potential predicts wrongly the B2 phase as the GM for CuZr at the 1:1 composition. Cheng *et al.* [60] have shown that the B2 phase is energetically more favored compared to the phase segregation products, $Cu_{10}Zr_7$ and $CuZr_2$ crystals. In reality, the B2 phase

is a high temperature phase of $Cu_{50}Zr_{50}$ produced during the initial devitrification for $Cu_{50}Zr_{50}$ [31] and $Cu_{48}Zr_{48}Al_4$ [32] metallic glasses, and it will transform to the segregated products $Cu_{10}Zr_7$ and $CuZr_2$. This incorrect prediction from EAM PES, however, should not affect the main purpose of this paper, which concerns the initial transition mechanism of glass towards the B2 phase.

Figure 2(b) shows that the DOS of minima increases dramatically and evolves into a broad peak starting from ~ 0.04 eV/atom. This implies that the global PES enters into the glassy region, where many energy-degenerate structures are available. To identify the key structural features of these glassy structures and distinguish them from crystalline structures, we have analyzed the structures for all the distinct minima. In particular, we calculated the coordination number (CN) for Cu and Zr. The CN centered on an atom i is defined in Eq. (2)

$$CN_i = \sum_j CN_{ij} = \begin{cases} 1, & r_{ij} \leqslant r_c \\ \frac{2(1-(r_{ij}/r_c)^{15})}{1-(r_{ij}/r_c)^{30}}, & r_{ij} \geqslant r_c \end{cases}, \quad (2)$$

where i and j are atom indices and r_c is 3.0 Å for CuZr. We found that the Zr-centered CN with Cu neighbors, i.e. $CN_{Zr(Cu)}$, differs noticeably between structures, and therefore, we always refer to CN_i as $CN_{Zr(Cu)}$ in the structural analysis of the CuZr system hereafter (thus, the index i represents Zr atoms, and the index j is summed over all Cu atoms). Based on that fact, we introduce two quantities to quantitatively distinguish the glassy

structures from the crystalline structures, namely the crystal similarity (CS) index and the coordination standard deviation (CSD) index, which can be calculated for each structure on PES according to Eqs. (3) and (4) (the index i is summed over all the Zr atoms; n is the number of Zr atom, i.e. $n = 8$ for the 16-atom Cu-Zr system)

$$\text{CS} = \frac{1}{n} \sum_i e^{-\frac{(\text{CN}_i - \text{CN}_{\text{cry}})^2}{2\sigma^2}}, \tag{3}$$

$$\text{CSD} = \sqrt{\frac{1}{n-1} \sum_i (\text{CN}_i - \overline{\text{CN}_i})^2}. \tag{4}$$

In Eq. (3), the Gaussian width $\sigma = 0.05$ and CN_{cry} are set as that of the B2 phase, $\text{CN}_{\text{B2}} = 8.01$. The CS therefore describes the structural similarity between a structure and the B2 crystal phase; the CSD describes the homogeneity of a structure as measured by CN. Following this, a CS $= 1$ and CSD $= 0$ indicates a perfect B2 lattice, with deviations lowering CS and increasing CSD in general. In Fig. 2(c), we plot the CS and CSD averaged over all structures in an energy interval, $(E, E + dE)$, against the energy E.

Figure 2(c) shows that the average CS drops, but average CSD increases obviously with the increase of energy. At high energies, the average CS is low, but the average CSD is high, indicating these high-energy structures deviate far from the B2 phase and become structurally heterogeneous. These two quantities can reflect the structural change during the transition from the crystalline structures to glassy structures and thus can be exploited to distinguish crystals and glassy structures. From Figs. 2(b) and 2(c), we may define the glassy structures for CuZr using the following energy and structure conditions:

$$E_{\text{g-c}} > 0.045 \, \text{eV/atom}, \tag{5}$$

$$\text{CS} < 0.21, \tag{6}$$

$$\text{CSD} > 1, \tag{7}$$

where $E_{\text{g-c}}$ is the energy gap between the glassy structures and the crystalline structure B2. The PES enters into the glassy region above 0.045 eV/atom, where the structures satisfying the structural conditions in Eqs. (6) and (7) have a continuous distribution in the DOS, as shown in Fig. 2(b) (red curve). It is clear that the high-energy structures do not necessarily belong to the glassy structures, which are often defected crystalline structures.

Three representative low-energy structures of glassy structures are selected, named as gs-1, gs-2, and gs-3, for further pathway studies (the next section). Figure 1(e) illustrates the atomic structure of gs-3, and those of gs-1 and gs-2 are shown in Supplemental Material Fig. S6 [45]. In the gs-3, the Zr atom with the lowest Cu coordination (4.07) is indicated by the arrow, which is much lower than the value (8.01) of the B2 crystal phase.

To examine the short-range ordering of the CuZr structures on the global PES, we have searched for the well-shaped icosahedron $\langle 0,0,12,0 \rangle$ Voronoi cluster, which is known to be critical for glass forming ability [25]. As compared in Fig. 2(d), there are a considerable number of icosahedral structures (521 structures with a $\langle 0,0,12,0 \rangle$ cluster among all 3021 structures), as indicated by the red dots, particularly in the

high-energy region above $\sim$0.05 eV/atom. These results are consistent with those obtained by MD and RMC simulations [25]. We have particularly examined the low-energy glassy structures in the energy range of 0.045–0.06 eV/atom, which contains in total 26 glassy structures. In these structures, four of them have a $\langle 0,0,12,0 \rangle$ Voronoi cluster, and five of them have other distorted icosahedron clusters, including $\langle 0,2,8,2 \rangle$ and $\langle 0,3,6,3 \rangle$.

B. Lowest energy pathways from glassy structures to crystalline structures

With all important minima identified, our next task is to find the lowest energy pathways connecting glassy structures with crystalline structures, which can help deduce the kinetics between structures. The kinetics data should be a quantitative measure for the glass forming ability of CuZr. This is facilitated by the recently developed iterative SSW reaction pathway sampling. It should be emphasized that the traditional approach for understanding the pathway in the crystallization is via the quenching of MD trajectories, where no clear barrier height can be obtained [28–30].

By using the iterative SSW reaction sampling method, we have searched the low-energy pathway starting from three low-energy glassy structures (gs-1, gs-2, and gs-3) and ending with the crystal B2 phase. These low-energy glassy structures, gs-1 to gs-3 as indicated in Figs. 2(a)–2(d), are $0.045 \sim 0.05$ eV above the B2 crystal and differ largely in the local atomic arrangement from the crystalline structures.

Typically, for each pathway between the glassy structure and the B2 phase, the iterative SSW reaction sampling needs to visit more than 10^6 minima and connect $\sim$5000 pathways between them until the lowest energy pathway is found. As a representative, we show the lowest energy pathway for the gs-3-to-B2 transition obtained after 18 cycles in SSW reaction sampling in Fig. 3. The other lowest reaction pathways from gs-1 and gs-2 to the B2 crystal phase are shown in Supplemental Material Fig. S6 [45].

Figure 3 shows that the gs-3-to-B2 pathway has a long transition path, bypassing five intermediates named from MS-A to MS-E. The overall barrier is 0.048 eV/atom, which is dictated by the TS (TS-2) in between MS-A and MS-B (the overall barriers of crystallization for gs-1 and gs-2 are 0.069 and 0.061 eV/atom, respectively, see Supplemental Material Fig. S6 [45]). This indicates that the escape from the glassy minimum is highly kinetically prohibited. The second highest barrier step occurs from MS-E to GM, being 0.044 eV/atom. The energy profile in Fig. 3 shows that the glassy structure gs-3 is separated from the B2 crystal phase by high-energy TSs, which is the same for other glassy structures studied (see Supplemental Material [45]).

We can better understand the energetic profile by inspecting the atomic displacement during the phase transition. In Fig. 3(b), the movement of the Zr7 atom, the Zr atom with the lowest Cu coordination as labeled in the figure, and its nearest neighbors are focused upon. From gs-3 to MS-B, the relative movement of Zr6, Zr7, and Zr8 on the (001) plane (all directions are referred to that in the B2 phase) are obvious, which creates a vacant site among them [the circle region in Fig. 3(b) MS-B]. From MS-B to MS-D, the nearby Cu
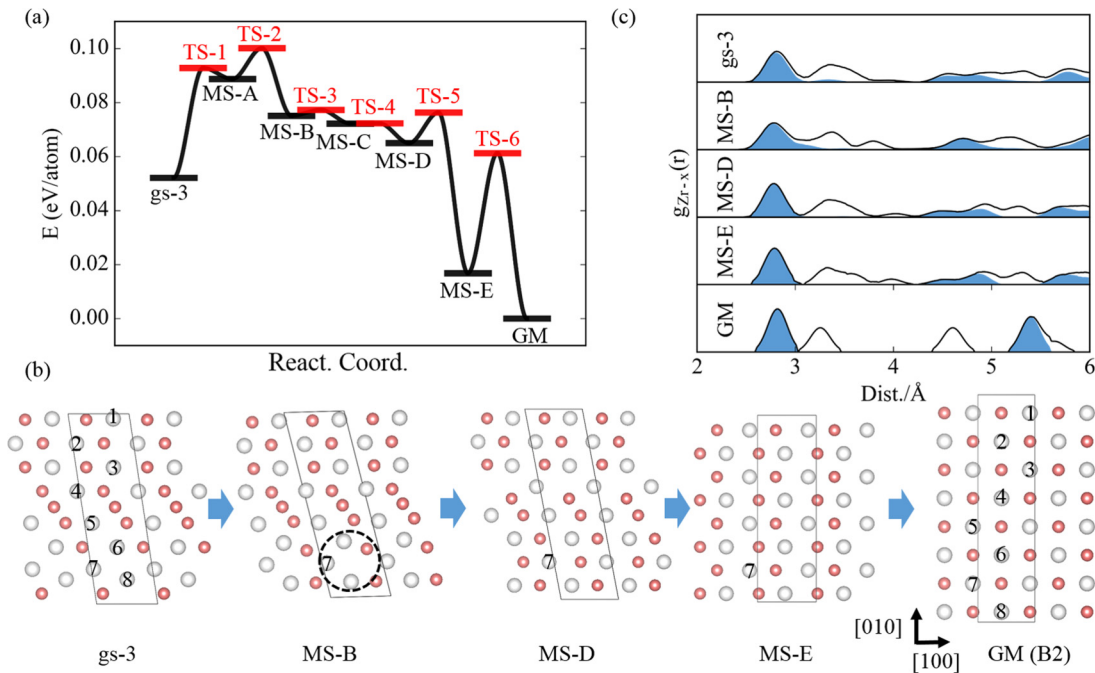
FIG. 3. (a) Reaction energy profile for the lowest energy pathway from the glassy structure gs-3 (as shown in Fig. 2) to the B2 crystal (GM). MS-A to MS-E are the intermediates structures; TS-1 to TS-6 are the TSs. (b) Structure snapshots for the key states along the reaction pathway. The circle in MS-B indicates the cavity created near Zr7. (c) Total RDF, $g_{Zr-X}(r)$ ($X = $ Zr and Cu) and partial RDF, $g_{Zr-Cu}(r)$ (blue shaded), for the intermediate states along the reaction pathway.

atoms start to move into this vacant site, and thus, the Zr7 increases two extra Cu CN (this is due to the periodic boundary conditions in our simulation) at the MS-D. In the final steps from MS-D to B2 crystal, the first shell of Zr7 arranges locally and evolves finally into a body-centered cubic (bcc) structure, B2 crystal. Our results show that the characteristics of local atomic displacement determines the kinetics of the glass-to-crystal transition. This is in line with the results from Fan *et al.* [27], who showed that the thermally activated deformation of the Cu$_{56}$Zr$_{44}$ system involves fewer than 30 atoms.

To have an overview on the structure evolution, we have plotted the radial distribution function (RDF) for the Zr atom g(Zr) in lattice along the reaction pathway, as shown in Fig. 3(c). For the final B2 phase, there are five major peaks up to 6 Å distance away from Zr centers, being around 2.85, 3.25, 4.65, 5.4, and 5.65 Å. The first and second peaks are related to Zr-Cu and Zr-Zr bondings, respectively, where the $g_{Zr-Cu}(r)$ RDF is blue colored to distinguish it from the $g_{Zr-Zr}(r)$ RDF. By contrast, for the initial glassy structure gs-3, the RDF is very broad and continuous starting from 2.8 Å. The nearest neighbor peak of Zr is centering at 2.9 Å, which contains both Zr-Zr and Zr-Cu bondings. It is also obvious that the peak height is much lower than those in the crystal B2 phase [65]. These structural features are clear indications for the glassy nature of gs-3.

Ongoing from gs-3 to B2, we observe that the intermediate structures, e.g. MS-B, have similar RDFs as the gs-3, with broad peaks starting from 3 Å and the Zr-Zr bond in the first shell. The shape of the RDF curve changes significantly in MS-D: the Zr-Zr bonds inside the first shell disappear, and the first peak of Zr-Cu bonds becomes sharper. The MS-E structure already has a relatively sharp first peak in RDF,

similar to that of GM, but the Zr-Zr RDF remains broad, smearing from 3.2 to 4 Å.

From Figs. 3(b) and 3(c), we can identify two major stages in the glass-to-crystal phase transition: Stage 1, gs-3 to MS-D, and Stage 2, MS-D to B2. Both stages contain a high barrier step, which can be attributed to the relative movement of Zr and Cu atoms. In the first stage, gs-3 to MS-D, the volume increases by 1.5% (MS-D has the largest volume along the pathway, see Supplemental Material Fig. S5 [45]), and Cu atoms in the second neighbor shell of Zr atom moves into the first neighbor shell, which increases the Zr7 CN from 4.07 to 6.01. In the MS-D to B2, the volume drops, and Cu atoms in the first neighbor shell of Zr atom pack into a body-centered bonding shell, which further increases the Zr7 CN from 6.01 to 8.01. Similar to the LJ particle crystallization PES identified by de Souza and Wales [37], the CuZr crystallization pathway in Fig. 3 shows a long plateau (gs-3 to MS-D, Stage 1) at high energies, which is followed by a fast drop in energy to MS-E. Such a cascade deformation (fast drop in energy) has been analyzed by Fan *et al.* [27] in the Cu$_{56}$Zr$_{44}$ system, which occurs often at the higher energy region with a higher density of local minima (MS-A to MS-D). Overall, it is clear that the glass-to-crystal phase transition involves obvious short-range Zr/Cu diffusion/exchange inside the solid, also known as the cage-breaking event [35,36], which causes the high barrier of transition.

It is worth mentioning that, by using discrete path sampling, Calvo *et al.* [34], de Souza and Wales [35–37], and Niblett *et al.* [38] also studied the reaction barriers from glassy states to the crystalline states in model glass former systems. One major difference in technique is that the current SSW method can relax the lattice of supercells during the pathway searching
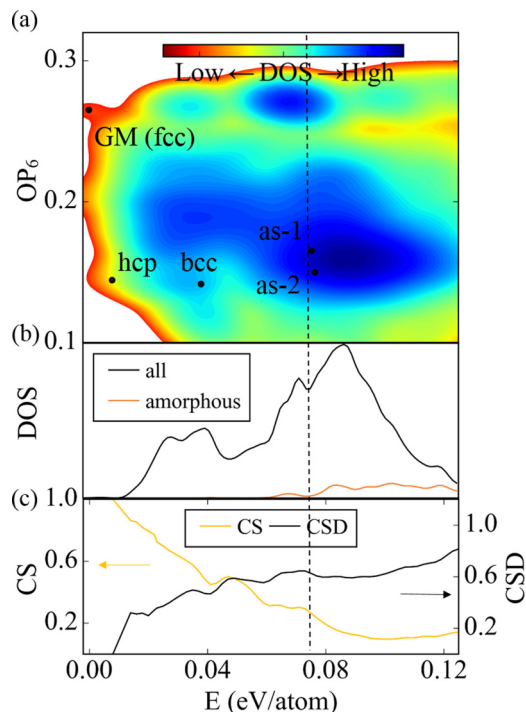
FIG. 4. (a) Global PES for pure Cu system (32-atom supercell), where the energy of structure (minimum) is plotted against the order parameter OP_6. (b) 1D DOS profile for all Cu structures (black curve) as appeared in (a), and for the selected structures satisfying the structural conditions of Eqs. (9) and (10) (red curve). (c) CS and CSD [see Eqs. (3) and (4)] profile of the Cu system to show the structure evolution from crystal to amorphous. The dashed line indicates the energy condition Eq. (8) to separate the amorphous structures from the crystalline structures.

[47,55,56], and thus, the barrier from SSW can better represent the solid-to-solid transition kinetics.

C. Pure Cu nonglassy system

To provide deeper insights into the glassy nature CuZr, we have also studied the global PES of the pure Cu system for comparison, which is known to be a nonglassy material. Similarly, we have utilized the SSW method to explore the Cu PES (in a 32-atom supercell). While more than 10^5 minima on PES are visited, there are only 6544 distinct minima that can be distinguished according to their energy, the space group, and Steinhardt-type order parameter [59]. In Fig. 4(a), we have shown the contour plots for the DOS of all distinct minima on Cu global PES, where the energy of each structure (eV/atom) is plotted against its Steinhardt-type order parameter with degree $l = 6$. The 1D DOS for the minima is shown in Fig. 4(b).

From the Cu PES, we can identify a number of high-symmetry crystalline structures. The most stable crystal structure, GM, is a face-centered-cubic (fcc) phase ($Fm\bar{3}m$, #225), in accordance with experiment, which is set as the energy zero. In the fcc structure, each Cu is surrounded by 12 Cu atoms, CN = 12.16 using Eq. (2) with $r_c = 2.7$ Å. There are also less stable crystalline structures with high symmetry, the hexagonal-close-packed (hcp; $P63/MMC$, #194) phase that

is 0.004 eV/atom above GM, the bcc ($Im\bar{3}m$, #229) phase that is 0.038 eV/atom above GM. These structures are shown in Supplemental Material Fig. S7 [45].

We then analyzed the atomic structures of all the distinct minima to identify the amorphous structures. The CN for Cu and the two indexes, CS and CSD, are also calculated for each structure in the Cu system using Eqs. (2)–(4). The parameters utilized are $\sigma = 0.05$ and $CN_{cry} = 12.16$ for fcc Cu GM. We find that the trend of the structure evolution is quite similar to that in the CuZr system: the average CS index decreases, and the average CSD index increases, as shown in Fig. 4(c), which are indications that the structure becomes amorphous with the increase of energy. According to the curves of CS and CSD, we can define roughly the amorphous structures using the following three conditions:

$$E_{g\text{-}c} > 0.075 \, \text{eV/atom}, \tag{8}$$

$$CS < 0.28, \tag{9}$$

$$CSD > 0.7. \tag{10}$$

The PES enters into the amorphous region above 0.075 eV/atom, where the structures satisfying the structural conditions in Eqs. (9) and (10) have a continuous distribution in the DOS, as shown in Fig. 4(b) (red curve).

It might be mentioned that, to choose suitable criteria for Cu in Eqs. (8)–(10), we have tested several possible sets of values as identified from Fig. 4(b), including energy from 0.05 to 0.075 eV/atom. By using these values, we can screen out a set of "amorphous structures" and validate the parameters by visualizing these selected amorphous structures, particularly for those just above the criteria. We found that, if the 0.05-set parameters are chosen, the amorphous structures contain a significant number of defective crystalline states, indicating that the energy is still too low to distinguish the true amorphous structures from the crystalline structures.

If comparing Fig. 4(b) (Cu system) with Fig. 2(b) (CuZr system), one can see immediately the most salient difference between two systems: the amorphous structures in the Cu system (red curve) have a very small population in the DOS of high-energy structures. In fact, most high-energy structures in the Cu system are either crystalline structures with mixed hcp, fcc, and bcc phases, or crystalline structures with point defects. However, the glassy structures contribute significantly to the high-energy structures in the CuZr system. Two low-energy amorphous structures have been selected, named as as-1 and as-2 [Fig. 4(a)], which are 0.075 and 0.076 eV/atom above GM, respectively. Similarly, we utilized the SSW reaction sampling to search for the transition pathway of crystallization. Interestingly, we find that both pathways have extremely low barriers of crystallization, which is in contrast with that of the CuZr system. The overall barrier for as-1 is lower than 0.001 eV/atom, while that for as-2 is 0.011 eV/atom.

Taking the lowest energy pathway from as-1 to GM as an example (the pathway for as-2 is detailed in Supplemental Material Fig. S9 [45]), we show the reaction profile and the snapshots in Fig. 5 . The reaction consists of two elementary steps with only one intermediate MS-A. In the transition, the Cu atoms at the as-1 need to displace locally, which leads to the increase of the Cu lowest CN (see Supplemental Material Fig. S8 [45]) from 10.20 in as-1 to 10.37 in MS-A and to
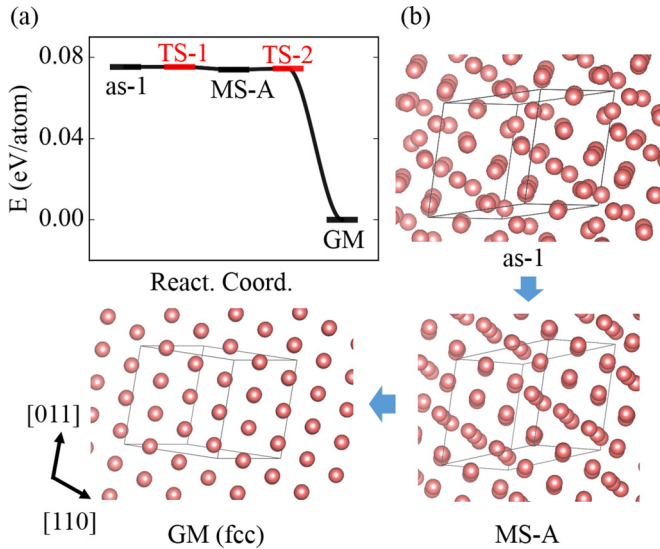
FIG. 5. (a) Energy profile the pathway connecting as-1 to fcc GM in the Cu system. (b) Structure snapshots for the as-1, MS-A, and GM along the reaction pathway.

FIG. 6. Evolution of the averaged RDF for (a) the Cu system $g_{Cu}(r)$ and (b) the CuZr system $g_{Zr-X}(r)$ ($X =$ Cu and Zr) with the increase of energy. The averaged g(r) at an energy E is calculated by averaging the g(r) over all structures in a small energy interval, $(E, E + 0.01)$ (eV/atom). The energy E is indicated in the top right corner of each plot. The averaged partial RDF, $g_{Zr-Cu}(r)$, is blue shaded in the CuZr system.

12.16 in GM. The volume decreases continuously through the reaction (see Supplemental Material Fig. S8 [45]).

IV. GENERAL DISCUSSIONS

A. Role of Zr atoms to the GFA of the CuZr system

The Cu:Zr composition is known to affect greatly the glass forming ability [9]. While the physical origin for the Zr role on glass forming ability remains largely elusive, the direct comparison of Zr concentration between local glassy structures and crystalline structures is often made to understand the glass forming ability differences. Wang *et al.* suggests that the change of Zr concentration may facilitate the formation of denser glassy structures [66,67] and the increase of the structural incompatibility between the glassy structures and their competing crystalline phases [67]. These are expected to increase the glass forming ability of material. For example, the glass forming ability of $Cu_{64.5}Zr_{35.5}$ is shown to be better than $Cu_{61.8}Zr_{38.2}$ [9]. This is attributed to the fact that the 64.5:35.5 ratio is far from the major crystalline phases with the 51:14 ratio ($Cu_{51}Zr_{14}$) [67] in $Cu_{64.5}Zr_{35.5}$. This explanation, however, meets with difficulty in rationalizing the good glass forming ability of $Cu_{50}Zr_{50}$, where the crystalline phase with the same CuZr composition, B2 phase as observed in experiment, acts as the key nucleation center.

By mapping out global PES, we show that $Cu_{50}Zr_{50}$ binary alloy exhibits obvious glassy characteristics, while pure Cu is nonglassy. Microscopically, we find that the glassy structures of $Cu_{50}Zr_{50}$ are inhomogeneous with the local Cu:Zr ratio deviating from 1:1. In other words, Zr atoms do prefer to enter into the first shell of other Zr atoms in the glassy structures, which reduces the Zr coordination with Cu [see Fig. 2(e)]. This can be illustrated clearly using the energy-resolved Zr-centered RDF in Fig. 6. The Zr-centered RDF $g_{Zr-X}(r)$ ($X = $ Zr,Cu) at an energy E is calculated by averaging the RDF over all structures in a small energy interval, $(E, E + 0.01)$ (eV/atom).

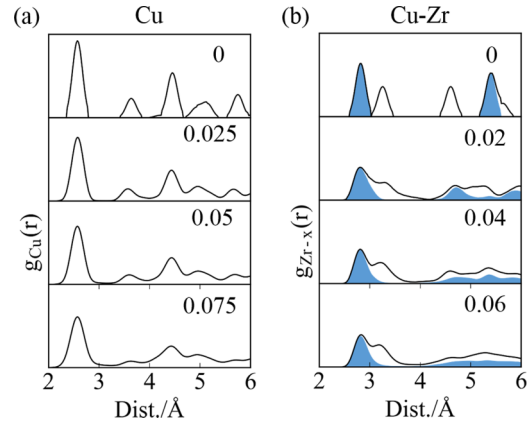As shown, when the energy increases from 0 to 0.06 eV/atom (the $Cu_{50}Zr_{50}$ system transits from crystal to glass), the second RDF peak in the crystalline structures, corresponding to the Zr-Zr distance peak, spreads out gradually and merges with the first peak as early as above 0.02 eV/atom. This indicates that new Zr-Zr bonds evolve in the glassy structures. The high-energy barrier associated with the movement of Zr atoms leads to the stability of the glassy structures and thus explains the good glass forming ability of the $Cu_{50}Zr_{50}$ system.

On the other hand, for the pure Cu system, we find that the RDF of the crystalline Cu has only a single sharp peak below 3 Å, corresponding to the Cu-Cu bond. This first peak also spreads out with the increase of energy, but it remains far away from the second peak even at high energies (0.075–0.085 eV/atom). This indicates that the local coordination of Cu, although being different at high energies, can be restored facilely since the atoms in the first neighboring shell are kept largely during the crystal-to-amorphous transition.

In accordance with the Zr-Cu coordination exchange from glass to crystal, we also find that the glassy structures in CuZr are quite condense, i.e. have a low volume expansion compared to the B2 crystal. There is only ~1% volume increase from GM to gs-3 in the pathway shown in Fig. 3, despite the large coordination change during the reaction. This density change falls within the data reported in experiment (~1% by Calvayrac *et al.* [68]; ~3% by Li *et al.* [66]). On the other hand, the Cu amorphous structures, both as-1 and as-2, have a large volume increase (by ~3%) compared to the Cu fcc crystal (see Supplemental Material for all the structures [45]).

By comparing the RDF plots from Cu and CuZr, we can conclude that the coalescence of the first and the second peaks is a unique feature in the CuZr transition from crystal to glass. The Zr atoms prefer to bond with Cu in the crystalline structures, but can also develop Zr-Zr bonds achieved by swapping Zr and Cu atoms with a low cost thermodynamically. Such a short-range Zr atom movement in solid states has a
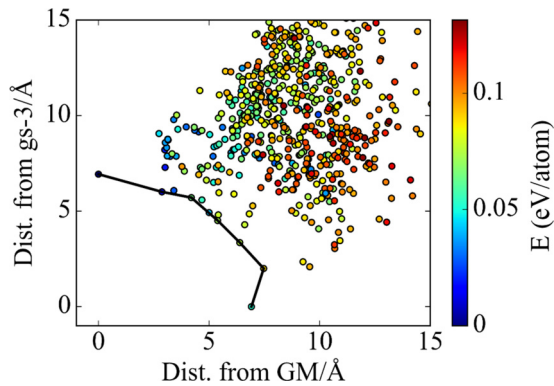
FIG. 7. Distance-distance map for the structures on PES relative to the B2 GM (*x* axis) and to the gs-3 (*y* axis) in the CuZr system. The lowest energy pathway shown in Fig. 3 is linked by the lines. All the distances are directly available from SSW iterative reaction pathway sampling, and the equations to calculate the distance between a pair of periodic structures can be found in Supplemental Material Part 2 [45]. The relative energy of each structure is indicated by the color scheme.

high-energy barrier, as shown from our pathway calculations, which effectively stabilizes the glassy structures of CuZr.

B. General differences between glassy and nonglassy systems

The SSW global optimization provides an opportunity to compare directly the glassy and nonglassy systems based on the global PES data. We can outline four major distinctions as follows:

(i) There are much more distinct minima on the global PES for glassy $Cu_{50}Zr_{50}$ compared to nonglassy Cu. Our SSW shows that, in the 16-atom supercell, the number of the distinct minima in the CuZr system is 3021, more than three times larger than that in Cu; in the 32-atom supercell, the number of the distinct minima in the CuZr system is 52716 (see Supplemental Material Fig. S1 [45] for the global PES), more than seven times larger than that in Cu. This indicates a much more corrugated PES for the glassy system, which benefits the formation of glass upon cooling from high temperatures.

(ii) The energy gap between glassy/amorphous structures and crystal GM is ∼0.045 eV/atom for glassy $Cu_{50}Zr_{50}$, which is much smaller than the value ∼0.075 eV/atom for nonglassy Cu. This is proof that the glassy structures are kinetically stable amorphous structures.

(iii) The reaction barrier towards crystallization in the glassy CuZr system (>0.048 eV/atom) is much higher than that (<0.011 eV/atom) in the nonglassy Cu system. This prevents the devitrification at low temperatures and yields the kinetic stability of glassy states.

(iv) The atom movement pattern in the crystallization pathway is much more complex for the glassy CuZr system compared to that for the nonglassy Cu system. This is in line with the high barrier mentioned in (iii).

To illustrate (iv) above, we have plotted the distance of the structures on PES with respect to the gs-3 and to the B2 GM in Fig. 7. The total length for the lowest energy pathway (in Fig. 3) is 15.54 Å, involving five intermediates, although the

direct distance between gs-3 and B2 is only 6.91 Å. This is apparently due to the fact that the creation of a cavity near Zr7 is required to break the Zr-Zr bonds before the nearby Cu atoms can move into the first shell of Zr7. On the other hand, the amorphous structures in the Cu system can link to the fcc/hcp crystal within two steps, where the reaction pathway is generally short and straight. The overall pathway length, for example, from as-1 to Cu fcc GM is only 5.41 Å (see Supplemental Material Fig. S8 [45]), where Cu atoms displace locally during the crystallization.

V. CONCLUSIONS

The glassy solids represent a large class of kinetically stable solid materials that lack long-range ordering. This paper represents a comprehensive survey on the atomic structures and kinetics stability of the binary metallic glass CuZr system by establishing the global PES from theory. Novel theoretical methods based on the SSW global optimization are utilized to explore the PES of the glassy CuZr system and the nonglassy Cu system and to identify the lowest energy pathway from the glassy/amorphous structures to the crystalline structures. Quantitative data are obtained to distinguish the glassy CuZr from the nonglassy Cu system, which can be summarized briefly as follows. Compared to the nonglassy system:

(i) The glassy system has a higher number of distinct minima on the global PES;

(ii) The glassy system has a much smaller energy gap between the crystalline structure and the glassy/amorphous structure;

(iii) The glassy system has a much higher reaction barrier in crystallization from glassy/amorphous structures due to the local position exchange of atoms.

While previous papers have correlated the vitrification kinetics with the atom diffusion events in model LJ systems [37], this paper moves on to obtain the detailed knowledge on the global PES for bimetallic materials by using the SSW global optimization method. The SSW simulation can treat simultaneously the atom and cell movements (with flexible volume) and is able to identify the solid-to-solid phase transition pathways. It can visit a large area of PES with a relatively low computational cost. To be more specific, we estimate that a SSW run for 10^6 minima (each minima requires ∼300 force/energy calculations) takes roughly the same computational cost for a MD simulation of 600 ns with a time step of 2 fs as measured by the number of energy/force evaluation steps, often the most computationally intensive part of simulation. This has not taken into account the highly parallel nature of SSW global optimization. While SSW runs at such a scale can already achieve a reasonable overview on the global PES for a material, a traditional MD run of ∼600 ns may still be trapped in a few local minima (note that MD is often utilized for free energy calculations that are not the purpose of SSW global optimization). This feature of SSW global optimization allows a fast assessment and quantification of the structural and energetics of the glassy local structures based on a large number of distinct minima on PES. Because the prediction of the glass formation ability is

critical for the design of new glassy material, we believe that a quantitative way to obtain thermodynamic and kinetic data to distinguish the glassy structures from the crystalline structures proposed here could facilitate high-throughput material design efficiently in the near future.

[1] W. Klement, R. H. Willens, and P. Duwez, Nature **187**, 869 (1960).

[2] A. L. Greer, Science **267**, 1947 (1995).

[3] W. H. Wang, Adv. Mater. **21**, 4524 (2009).

[4] P. Chaudhari and D. Turnbull, Science **199**, 11 (1978).

[5] G. Kumar, A. Desai, and J. Schroers, Adv. Mater. **23**, 461 (2011).

[6] G. Kumar, H. X. Tang, and J. Schroers, Nature **457**, 868 (2009).

[7] B. Zberg, P. J. Uggowitzer, and J. F. Loeffler, Nat. Mater. **8**, 887 (2009).

[8] J. Schroers, Adv. Mater. **22**, 1566 (2010).

[9] D. Wang, Y. Li, B. B. Sun, M. L. Sui, K. Lu, and E. Ma, Appl. Phys. Lett. **84**, 4029 (2004).

[10] D. H. Xu, B. Lohwongwatana, G. Duan, W. L. Johnson, and C. Garland, Acta. Mater. **52**, 2621 (2004).

[11] A. Inoue and W. Zhang, Mater. Trans. **45**, 584 (2004).

[12] W. H. Wang, J. J. Lewandowski, and A. L. Greer, J. Mater. Res. **20**, 2307 (2011).

[13] G. Duan, D. H. Xu, Q. Zhang, G. Y. Zhang, T. Cagin, W. L. Johnson, and W. A. Goddard, Phys. Rev. B **71**, 224208 (2005).

[14] J. D. Bernal, Nature **185**, 68 (1960).

[15] P. H. Gaskell, Nature **276**, 484 (1978).

[16] D. D. Kofalt, S. Nanao, T. Egami, K. M. Wong, and S. J. Poon, Phys. Rev. Lett. **57**, 114 (1986).

[17] J. P. K. Doye and D. J. Wales, Science **271**, 484 (1996).

[18] F. Spaepen, Nature **408**, 781 (2000).

[19] D. B. Miracle, Nat. Mater. **3**, 697 (2004).

[20] H. W. Sheng, W. K. Luo, F. M. Alamgir, J. M. Bai, and E. Ma, Nature **439**, 419 (2006).

[21] Y. Q. Cheng and E. Ma, Prog. Mater. Sci. **56**, 379 (2011).

[22] A. Heuer, J. Phys.: Condens. Matter. **20**, 373101 (2008).

[23] M. Li, C. Z. Wang, S. G. Hao, M. J. Kramer, and K. M. Ho, Phys. Rev. B **80**, 184201 (2009).

[24] J. L. Finney, Proc. R. Soc. A **319**, 479 (1970).

[25] Y. Q. Cheng, H. W. Sheng, and E. Ma, Phys. Rev. B **78**, 014207 (2008).

[26] N. Jakse and A. Pasturel, Appl. Phys. Lett. **93**, 113104 (2008).

[27] Y. Fan, T. Iwashita, and T. Egami, Phys. Rev. Lett. **115**, 045501 (2015).

[28] S. Sastry, P. G. Debenedetti, and F. H. Stillinger, Nature **393**, 554 (1998).

[29] R. J. Speedy, J. Chem. Phys. **110**, 4559 (1999).

[30] S. Sastry, P. G. Debenedetti, F. H. Stillinger, T. B. Schroder, J. C. Dyre, and S. C. Glotzer, Phys. A **270**, 301 (1999).

[31] I. Kalay, M. J. Kramer, and R. E. Napolitano, Metall. Mater. Trans. A **42**, 1144 (2010).

[32] R. Wei, X. L. Wang, S. Yang, F. Jiang, and L. He, J. Alloy Compd. **617**, 699 (2014).

[33] T. F. Middleton and D. J. Wales, J. Chem. Phys. **118**, 4583 (2003).

[34] F. Calvo, T. V. Bogdan, V. K. de Souza, and D. J. Wales, J. Chem. Phys. **127**, 044508 (2007).

[35] V. K. de Souza and D. J. Wales, J. Chem. Phys. **129**, 164507 (2008).

[36] V. K. de Souza and D. J. Wales, J. Chem. Phys. **130**, 194508 (2009).

[37] V. K. de Souza and D. J. Wales, J. Stat. Mech. **2016**, 074001 (2016).

[38] S. P. Niblett, V. K. de Souza, J. D. Stevenson, and D. J. Wales, J. Chem. Phys. **145**, 024505 (2016).

[39] S. De, B. Schaefer, A. Sadeghi, M. Sicher, D. G. Kanhere, and S. Goedecker, Phys. Rev. Lett. **112**, 083401 (2014).

[40] G. A. Tomlinson, Philos. Mag. **7**, 905 (1929).

[41] C. Shang and Z.-P. Liu, J. Chem. Theory Comput. **9**, 1838 (2013).

[42] X.-J. Zhang, C. Shang, and Z.-P. Liu, J. Chem. Theory Comput. **9**, 3252 (2013).

[43] C. Shang, X.-J. Zhang, and Z.-P. Liu, Phys. Chem. Chem. Phys. **16**, 17845 (2014).

[44] X.-J. Zhang and Z.-P. Liu, Phys. Chem. Chem. Phys. **17**, 2757 (2015).

[45] See Supplemental Material at http://link.aps.org/supplemental/10.1103/PhysRevB.95.214111 for methodology and calculation details (SSW-RS method; formula to calculate distance between two structures in lattice); global PES in the 32-atom CuZr system; global PES in the 32-atom Cu system using the Cu potential taken from the CuZr potential; global PES in the 48-atom Cu system; structures of other low-energy crystal minima in the CuZr system; volume and coordination profile for the lowest energy pathway from gs-3 to B2 crystal in the CuZr system; lowest energy pathway from gs-1 and gs-2 to GM in the CuZr system; structures of low-energy crystal minima in the Cu system; volume, coordination profile, and distance-distance map for the lowest energy pathway from as-1 to fcc GM crystal in the Cu system; energy profile of pathway from as-2 to hcp crystal in the Cu system; *XYZ* structure coordinates for the structures.

[46] C. Shang and Z. P. Liu, J. Chem. Theory Comput. **8**, 2215 (2012).

[47] S. C. Zhu, S. H. Xie, and Z. P. Liu, J. Am. Chem. Soc. **137**, 11532 (2015).

[48] S. C. Zhu, S. H. Xie, and Z. P. Liu, J. Phys. Chem. Lett. **5**, 3162 (2014).

[49] Y. F. Li, S. C. Zhu, and Z. P. Liu, J. Am. Chem. Soc. **138**, 5371 (2016).

[50] S. H. Guan and Z. P. Liu, Phys. Chem. Chem. Phys. **18**, 4527 (2016).

[51] S. C. Zhu, S. H. Guan, W. N. Zhao, and Z. P. Liu, Top. Catal. **58**, 644 (2015).

[52] X.-J. Zhang and Z.-P. Liu, J. Chem. Theory Comput. **11**, 4885 (2015).

[53] X.-J. Zhang, C. Shang, and Z.-P. Liu, J. Chem. Theory Comput. **9**, 5745 (2013).

[54] N. Metropolis and S. Ulam, J. Am. Stat. Assoc. **44**, 335 (1949).

[55] S. H. Guan, X. J. Zhang, and Z. P. Liu, J. Am. Chem. Soc. **137**, 8010 (2015).

[56] Y. P. Xie, X. J. Zhang, and Z. P. Liu, J. Am. Chem. Soc. **139**, 2545 (2017).

[57] D. J. Wales, Mol. Phys. **100**, 3285 (2002).

[58] S. Plimpton, J. Comput. Phys. **117**, 1 (1995).

[59] P. J. Steinhardt, D. R. Nelson, and M. Ronchetti, Phys. Rev. B **28**, 784 (1983).

[60] Y. Q. Cheng, E. Ma, and H. W. Sheng, Phys. Rev. Lett. **102**, 245501 (2009).

[61] M. S. Daw and M. I. Baskes, Phys. Rev. B **29**, 6443 (1984).

[62] R. Ray, B. C. Giessen, and N. J. Grant, Scripta Metall. **2**, 357 (1968).

[63] J. Dudonis, R. Brucas, and A. Miniotas, Thin Solid Films **275**, 164 (1996).

[64] M. I. Mendelev, M. J. Kramer, C. A. Becker, and M. Asta, Philos. Mag. **88**, 1723 (2008).

[65] H. E. Fischer, A. C. Barnes, and P. S. Salmon, Rep. Prog. Phys. **69**, 233 (2006).

[66] Y. Li, Q. Guo, J. A. Kalb, and C. V. Thompson, Science **322**, 1816 (2008).

[67] X. D. Wang, S. Yin, Q. P. Cao, J. Z. Jiang, H. Franz, and Z. H. Jin, Appl. Phys. Lett. **92**, 011902 (2008).

[68] Y. Calvayrac, J. P. Chevalier, M. Harmelin, A. Quivy, and J. Bigot, Philos. Mag. B **48**, 323 (1983).